Controlling the rotation of asymmetric top molecules by the combination of a long and a short laser pulse

Simon S. Viftrup,[1] Vinod Kumarappan,[2,*] Lotte Holmegaard,[2] Christer Z. Bisgaard,[1,†] Henrik Stapelfeldt,[2,3,‡] Maxim Artamonov,[4] Edward Hamilton,[4] and Tamar Seideman[4,§]

[1]*Department of Physics and Astronomy, University of Aarhus, DK 8000 Aarhus C, Denmark*

[2]*Department of Chemistry, University of Aarhus, DK-8000 Aarhus C, Denmark*

[3]*Interdisciplinary Nanoscience Center (iNANO), University of Aarhus, DK-8000 Aarhus C, Denmark*

[4]*Department of Chemistry, Northwestern University, 2145 Sheridan Road, Evanston, Illinois 60208-3113, USA*

(Received 17 November 2008; published 4 February 2009)

We describe theoretically and experimentally a laser-based method to control the rotations of asymmetric top molecules in three-dimensional space. Our method relies on keeping one axis of a molecule essentially fixed in space along the polarization vector of a nanosecond laser pulse (termed the long pulse) and forcing the molecule to rotate about the aligned axis by an orthogonally polarized, femtosecond laser pulse (termed the short pulse). Experimentally, we use femtosecond timed Coulomb explosion to image the three-dimensional (3D) alignment of the 3,5-difluoroiodobenzene molecule as a function of time after the short pulse. Strong 3D alignment is observed a few picoseconds after the short pulse and is repeated periodically, reflecting directly the revolution of the molecular plane about the aligned axis. Our numerical results, based on nonperturbative solution of the time-dependent Schrödinger equation, are in good agreement with the experimental findings and serve to unravel the underlying physical mechanism of the observations. The experiments and theory explore the influence of the laser parameters on the rotational control, in particular the role played by the intensity of the long and the short laser pulses. To illustrate the generality of our method, we illustrate its applicability to a molecule (3,4-dibromothiophene), with significantly different inertia and polarizability tensors. Finally, our theory shows that the strong 3D alignment obtained by the combined laser pulse method can be converted in to field-free alignment by rapid truncation of the long laser pulse.

DOI: 10.1103/PhysRevA.79.023404 PACS number(s): 42.50.Hz, 33.15.Bh, 33.80.−b, 42.65.Re

I. INTRODUCTION

Laser alignment—the application of moderately intense laser pulses to align neutral molecules along the polarization axis(es) of a laser electric field—has grown over the past decade into an active research area with a broad variety of demonstrated and projected applications in areas such as ultrafast optics [1], x-ray absorption and diffraction [2,3], ultrafast imaging [4,5], high-order harmonic generation [6–9], molecular dynamics, and solution chemistry [10]. Although most studies to date have focused on the case of isolated rigid linear molecules subject to linearly polarized fields, recent research has generalized the method to asymmetric tops [11–13], solvated molecules [14], and surface-adsorbed molecules [15]; to complex systems such as small proteins [16] and molecular assembly and to new control opportunities [15]. Extensions of alignment to orientation [17–22] and to three-dimensional (3D) alignment [12,23–26] have been likewise fruitful research areas with a growing range of applications. Three-dimensional alignment, in particular, can be induced by an elliptically polarized field [23,26] or by the combination of two orthogonal fields [12,24,25]. In the polyatomic domain, it has enabled spatial control of asymmetric top molecules, which remain free to rotate about the field and molecular axes in linearly polarized fields. We omit discussion of the principle of alignment and 3D alignment (see Refs. [27,28] for an early and a recent review) and note here only that (1D and 3D) alignment can be induced adiabatically [27] by means of a long pulse, or nonadiabatically [27] by means of a short pulse (here and below "long" and "short" are meant with respect to the rotational periods of the studied molecule). In the former case, the alignment follows the pulse envelope and is lost upon the pulse turn-off, whereas in the latter dynamical alignment is available after the pulse turn-off, under field-free conditions.

A recent study combines experiments with theory to extend the concept of 3D alignment to complete control over molecular rotations by means of a combination of orthogonally polarized long and short pulses [25]. This pulse combination is shown to introduce the possibility of holding asymmetric tops in 3D space by application of the long, linearly polarized pulse, and next spinning them about the arrested molecular axis using the orthogonally polarized short pulse. The present work extends the theoretical and experimental work presented in Ref. [25] in several ways. Specifically, we explore the importance of strong initial 1D alignment for achieving strong 3D alignment by the combined fields, and the role of the short-pulse intensity. We also extend our study to explore two asymmetric top molecules that differ widely in properties. The first, 3,5-difluoroiodobenzene (DFIB), has rotational constants A_e=1750 MHz, B_e =484 MHz, and C_e=379 MHz, giving an asymmetry param-

*Present address: Department of Physics, Kansas State University, Kansas 66506, USA.

†Present address: Steacie Institute for Molecular Sciences, National Research Council, Ottawa, Ontario, Canada K1A 0R6.

‡henriks@chem.au.dk

§seideman@chem.northwestern.edu

eter $\kappa=(2B_e-A_e-C_e)/(A_e-C_e)=-0.847$. The second, 3,4-dibromothiophene (DBT), has rotational constants $A_e=949$ MHz, $B_e=946$ MHz, and $C_e=474$ MHz, with which $\kappa=0.987$. The two molecules differ also in their polarizability tensors: that of DFIB is similar to the polarizability tensor of iodobenzene, whose components along the principal inertia axes are $\alpha_a=21.5$ Å^3, $\alpha_b=15.3$ Å^3, and $\alpha_c=10.2$ Å^3. For DBT the computed polarizability components are $\alpha_a=16$ Å^3, $\alpha_b=20.6$ Å^3, and $\alpha_c=10.1$ Å^3.

The next section briefly outlines our experimental and numerical methods and Sec. III presents and discusses our results. The final section concludes with an outlook to future research.

II. METHODS

Both our experimental setup and our theory and numerical methods have been discussed in previous publications [28–30], and only a brief outline of aspects specific to the present application is presented in this section.

A. Experimental setup

A pulsed molecular beam, formed by expanding a few mbar DFIB and 90 bar helium into vacuum [30], is crossed at 90° by three pulsed laser beams. The short alignment pulses [150 fs full width at half maximum (FWHM), 800 nm, $\omega_0=50$ μm] are electronically synchronized to the peak of the long pulses (10 ns FWHM, 1064 nm, $\omega_0=50$ μm) with a time jitter$\leqslant\pm0.5$ ns. The probe pulses (30 fs FWHM, 800 nm, $\omega_0=30$ μm) are sent at a controllable time t after the center of the short pulse using an optical delay line. The probe pulses are sufficiently intense (3×10^{14} W/cm^2) that they can remove several electrons from the molecules, thereby triggering Coulomb explosion into ionic fragments. In particular, I^+ and F^+ fragment ions are useful experimental observables since they recoil along the C-I symmetry axis and in the plane of the molecule, respectively. The velocity vectors of both ion species are detected with two-dimensional ion imaging implemented by accelerating the ions with a weak static field toward a microchannel plate detector backed by a phosphor screen and recording the ion hit positions with a charge-coupled device (CCD) camera (780×582 pixels, but only 575×575 pixels are effectively used). This allows us to determine the instantaneous molecular orientation at the time of the probe pulse [30].

Ideally, the interaction between the (linearly polarized) probe pulse and each molecule should be independent of the molecular alignment—this would produce an orientationally uniform probe. In practice, however, this is not the case, as shown in a large number of studies of Coulomb explosion of molecules. In fact, the orientational selectivity of the ionization process can result in ion images that look aligned although the molecular orientations are isotropically distributed. Consequently, it is crucial to choose the polarization of the probe with respect to the detector plane such that possible misinterpretations of the recorded ion distributions regarding the molecular orientation is avoided.

For the DFIB molecules the production of I^+ ions is a function of the angle between the probe polarization and the molecular symmetry axis, with the ion yield being maximized in the parallel geometry case. As a result, we polarize the probe pulse perpendicular to the detector plane (Fig. 2, rows A and B). This ensures no angular selectivity in the detector plane, and therefore any deviations from the circularly symmetrical images obtained with the probe alone (Fig. 2, A1 or B1) identify alignment of the molecular C-I axis.

Similarly, the F^+ yield depends strongly on the angle between the C-I axis and the probe polarization axis: We observed ten times higher F^+ yield in the parallel compared to the perpendicular geometry. Furthermore, we observed that the yield of F^+ ions depends on the angle between the probe polarization and the molecular plane: Highest yield was observed when the polarization of the probe coincided with the molecular plane.

To minimize the orientational bias of the Coulomb explosion process and ensure that the F^+ angular distribution reflect as closely as possible the orientation of the molecular plane, we chose to polarize the probe pulse parallel to the long pulse polarization. The high degree of 1D alignment throughout the experiment efficiently removed the problems with probe selectivity, since the C-I axis of most molecules was at very low angle to the probe polarization. This explains our choice of probe pulse polarization parallel to the detector in the F^+ side view (Fig. 2, row C) and perpendicular to the detector in the F^+ end view (Fig. 2, row D).

B. Theory and numerical implementation

The complete Hamiltonian is written as

$$H=H_{\rm rot}+H_{\rm ind}^{l}+H_{\rm ind}^{s}. \tag{1}$$

The field-free Hamiltonian $H_{\rm rot}$ is approximated in the rigid rotor limit, i.e.,

$$H_{\rm rot}=\frac{\mathbf{J}_X^2}{2I_{XX}}+\frac{\mathbf{J}_Y^2}{2I_{YY}}+\frac{\mathbf{J}_Z^2}{2I_{ZZ}}. \tag{2}$$

$\mathbf{J}_k$, $k=X,Y,Z$, are the body-fixed components of the material angular momentum vector, and I_{kk} are the corresponding components of the inertia tensor. The induced dipole Hamiltonian for the long-, $H_{\rm ind}^{l}$, and short-, $H_{\rm ind}^{s}$, pulse interactions is given by

$$H_{\rm ind}^{j}=-\frac{1}{4}\sum_{\rho,\rho'}\varepsilon_{\rho}^{j}\alpha_{\rho\rho'}\varepsilon_{\rho'}^{j*} \tag{3}$$

(see the appendix of [28]), where $j=l,s$, $\rho,\rho'=x,y,z$ are the space-fixed coordinates, and $\boldsymbol{\alpha}$ is the molecular polarizability tensor. The field is written in the semiclassical approximation as

$$\boldsymbol{\varepsilon}^{j}(t)=\frac{1}{2}[\boldsymbol{\varepsilon}^{j}(t)e^{i\omega^{j}t}+\boldsymbol{\varepsilon}^{j*}(t)e^{-i\omega^{j}t}], \tag{4}$$

where $\boldsymbol{\varepsilon}^{j}(t)=\hat{\boldsymbol{\varepsilon}}\varepsilon^{j}(t)$, $\hat{\boldsymbol{\varepsilon}}$ is a unit vector in the field polarization direction, $\varepsilon^{j}(t)$ is the pulse envelope, and ω^{j} is the center frequency. The short pulse is Gaussian centered at time $t=0$ with the same duration as in the experiment.

Because of the large rotational period of DFIB, the long-pulse duration required to ensure an adiabatic turn-on (10 ns

in the experiment) makes it impractical to solve the corresponding time-dependent Schrödinger equation by time propagation from the onset of the long pulse to the onset of the short pulse. A more efficient approach is to start with the eigenstates of the adiabatic Hamiltonian, $H_{\text{adiab}}=H_{\text{rot}}+H^{l}_{\text{ind}}(t=0)$ (the pulses are centered at $t=0$), which are expanded in a complete set of the symmetric top eigenstates at the onset of the short pulse thus converting the time-dependent Schrödinger equation into a set of coupled first-order differential equations. The choice of the symmetric top basis set makes for an easy evaluation of the matrix elements of the complete Hamiltonian as well as the observables. After the short-pulse turn-off, the wave function is transformed back into the H_{adiab} representation since in this representation the time evolution is determined in a trivial way. However, the computational effort associated with direct diagonalization of the H_{adiab} matrix in the symmetric top representation rapidly grows prohibitive with an increase in the basis set size. Therefore from the numerical implementation point of view, it is convenient to define the space-fixed z axis as the long-pulse linear polarization direction. Cylindrical symmetry of the field about the space-fixed z axis leads to H_{adiab} being ϕ independent and, hence, to conservation of the magnetic quantum number M, i.e., the projection of $\mathbf{J}$ on the space-fixed z axis. Since M is now a good quantum number, the H_{adiab} matrix can be rearranged in a block-diagonal form. The blocks are diagonalized independently of each other (and in principle in parallel) resulting in a significant reduction in the overall computational effort and memory requirements.

The issue of numerical efficiency arises also in the solution of the time-dependent Schrödinger equation when the short pulse is on. In this stage of the calculation the wave function is represented as a superposition of the symmetric top eigenstates and most of the computational cost is in the evaluation of the matrix elements of the complete Hamiltonian. We considerably improve numerical efficiency in this stage by eliminating the need to reevaluate these matrix elements during the time propagation. The H_{rot} matrix is tridiagonal (for an asymmetric top molecule) and the H^{j}_{ind} matrices are sparse, albeit displaying a more complex structure. Thus, unique nonzero elements constitute only a fraction of the full matrix and can be precalculated and stored in memory to be recalled as needed.

We refer our results to two systems of axes, the one fixed in the laboratory and the other in the molecular frame—see Fig. 1. The space-fixed z and y axes are defined as the long- and the short-pulse polarization directions, respectively. The molecule-fixed Z axis is defined by the C-I bond axis and the body-fixed X axis lies in the molecular plane. With this definition perfect 1D alignment corresponds to $\theta=0,\pi$, where θ is the polar Euler angle between the space- and body-fixed z axes, whereas rotation about the C-I axis is described by the azimuthal Euler angle χ. We remark that our choice of coordinates differs from that of Ref. [25], where we defined the space-fixed xy plane by the polarization vectors of the long and short pulses. The present choice is dictated by our numerical implementation of the theory. The more efficient approach taken in the calculations below allow us to explore much larger systems than our earlier implementation, but does not allow the same flexibility in the choice of axis systems.

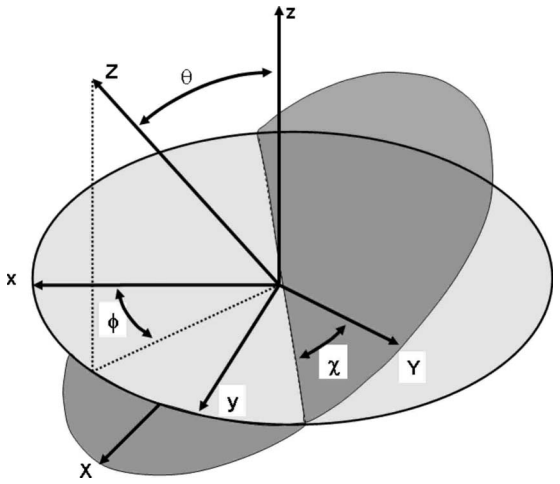

FIG. 1. Definition of the body-fixed (X,Y,Z) and space-fixed (x,y,z) coordinate systems in terms of the Euler angles that characterize their relative rotation. The space-fixed z and y axes are defined as the long- and the short-pulse polarization directions, respectively, the molecule-fixed Z axis is defined by the C-I bond axis and the body-fixed X axis lies in the molecular plane.

III. RESULTS AND DISCUSSION

A. Adiabatic alignment

We begin with a discussion of the adiabatic alignment of DFIB by means of a long pulse. Figure 2 B2 shows an I^+ image recorded with the long-pulse polarization perpendicular to the detector plane and the molecular orientation probed at the peak of the long pulse. The I^+ ions are localized in a circular range with a radius that is much smaller than the corresponding I^+ distribution obtained when no long pulse is included (Fig. 2 B1). This shows that the C-I axis of the

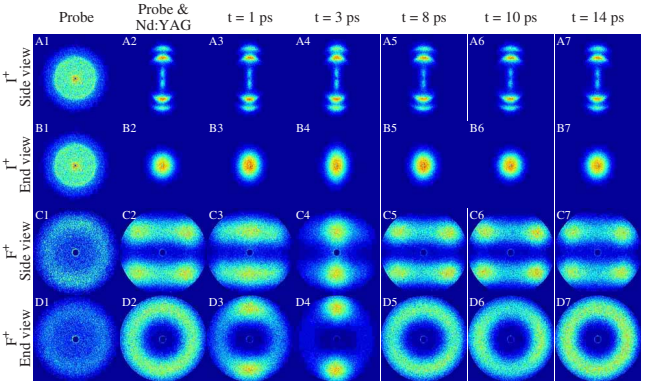

FIG. 2. (Color online) Ion images (as recorded by the CCD camera) of I^+ and F^+ fragments recorded in both end and side views. Column 1 (probe pulse only) and 2 (probe pulse and long pulse) serve as reference images. Columns 3–7, recorded at different times after the short pulse, illustrate the alignment dynamics. The intensities of the long and short pulses are 7×10^{11} and 2×10^{13} W/cm^2.

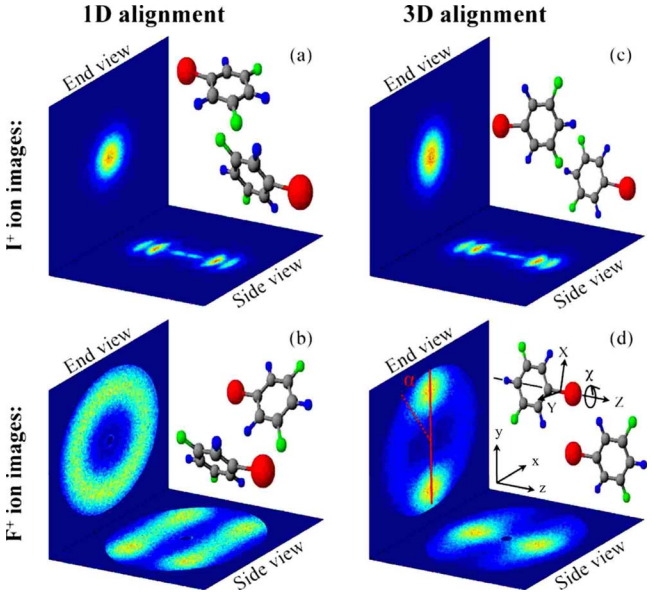

FIG. 3. (Color online) Illustration of the correspondence between the observed ion images and the spatial orientation of the DFIB molecules. End views (vertical panels) are obtained by polarizing the long pulse perpendicular to the detector plane and side views (horizontal panels) by polarizing the long pulse parallel to the detector plane. (d) shows the laboratory-fixed (x,y,z) and molecule (X,Y,Z) coordinate systems as well as two of the angles (χ,α) used to describe the alignment—see text.

molecules is strongly confined along the long-pulse polarization, i.e., the molecules are 1D aligned perpendicular to the detector. As a result, images obtained with the long pulse polarized perpendicular to the detector plane can be regarded as an "end view" (see Fig. 3). Similarly, when the long pulse is polarized parallel to the detector plane images correspond to a "side view" (see Fig. 3). In this geometry we can measure the degree of alignment using the expectation value $\langle\cos^2\theta_{2D}\rangle$, where θ_{2D} is the angle between the projection of the I^+ recoil velocity on the detector plane and the long-pulse polarization. For image A2 in Fig. 2 $\langle\cos^2\theta_{2D}\rangle=0.93$.

The 1D alignment is also visible in the F^+ images. In the absence of the long pulse the F^+ image, recorded in the end view, takes the form of a circularly symmetric disc (Fig. 2 D1). When the long pulse is included the circular symmetry is conserved but the F^+ ions emerge on a ring with no signal detected in the innermost central region (Fig. 2 D2). Such a ring structure is only compatible with the C-I axis being aligned perpendicular to the detector plane and the rotation of molecular plane uniformly distributed around the C-I axis. The F^+ side view is fully compatible with this conclusion. The axially aligned molecules will lead to F^+ ions ejected in two doughnut-shaped lobes centered along the long-pulse polarization. When projected on a plane containing the long-pulse polarization, corresponding to a side view, the two doughnut-shaped lobes should produce an image similar to that observed in the horizontal panel of Fig. 2 C2.

Figure 4 substantiates the results of Fig. 2, and generalizes them to an arbitrary asymmetric top by means of calculations. To that end we compute the expectation value of $\langle\cos^2\theta\rangle$ in an adiabatically excited rotational wave packet,

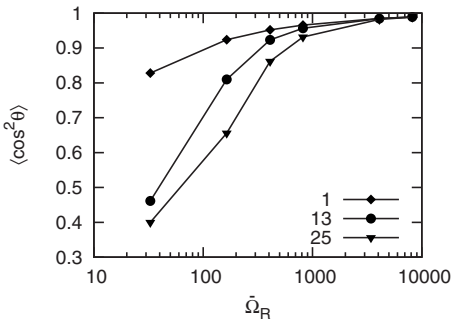

FIG. 4. Extent of one-dimensional alignment as a function of interaction strength for three values of the reduced temperature $\bar{T}=\bar{I}kT/\hbar^2$.

where θ is the angle between the space-fixed and body-fixed z axes (see Fig. 1) vs a dimensionless interaction parameter defined as

$$\bar{\Omega}_R=\frac{\bar{I}\bar{\alpha}\varepsilon^2}{4\hbar^2}. \tag{5}$$

In Eq. (5), $\bar{\alpha}$ is the trace of the polarizability tensor (the average polarizability), $\bar{\alpha}=(\alpha_{XX}+\alpha_{YY}+\alpha_{ZZ})/3$, and $\bar{I}=\frac{1}{2}(I^e_{XX}+I^e_{YY})$, where α_{kk}, $k=X,Y,Z$ are the Cartesian components of the polarizability tensor and I^e_{kk} are the corresponding components of the inertia tensor at the equilibrium configuration of the molecule. Our definition of the reduced parameters follows from a transformation of the Hamiltonian to a set of molecule- and field-independent interaction, time, and temperature variables that is discussed elsewhere [28] and is not elaborated on here. At practical intensities, the effect of the rotational temperature is dramatic, as was found experimentally and numerically before. In the strong-interaction limit, however, the temperature effect gradually diminishes. For the case of DFIB, the values of the reduced interaction parameter $\bar{\Omega}_R$ of 100 and 1000 correspond to the field intensities of 1.7×10^{10} and 1.7×10^{11} W/cm^2, respectively, while the reduced temperature values in Fig. 4 correspond to 0.04, 0.53, and 1.02 K.

Whereas $\langle\cos^2\theta\rangle_{2D}$ is a system-dependent observable that could be argued dependent on the probe, $\langle\cos^2\theta\rangle$ is a transferable measure of the alignment alone. Previous studies show that these two measures of alignment agree qualitatively [31,32]. Also, our results in the present work show that the former and the latter convey the same information.

B. Early-time dynamics

The next step is to control the orientation of the molecular plane. For this purpose a short pulse, polarized perpendicular to the long-pulse polarization, is applied at the peak of the long pulse. Focusing first on the end view F^+ images, it is seen that after the short pulse the initial circular symmetry is replaced by localization around the short-pulse polarization. The localization is prominent already at $t=1$ ps (Fig. 2 D3) and reaches a peak around $t=3$ ps (Fig. 2 D4). The strong confinement of the F^+ ions at $t=3$ ps shows that the molecu-

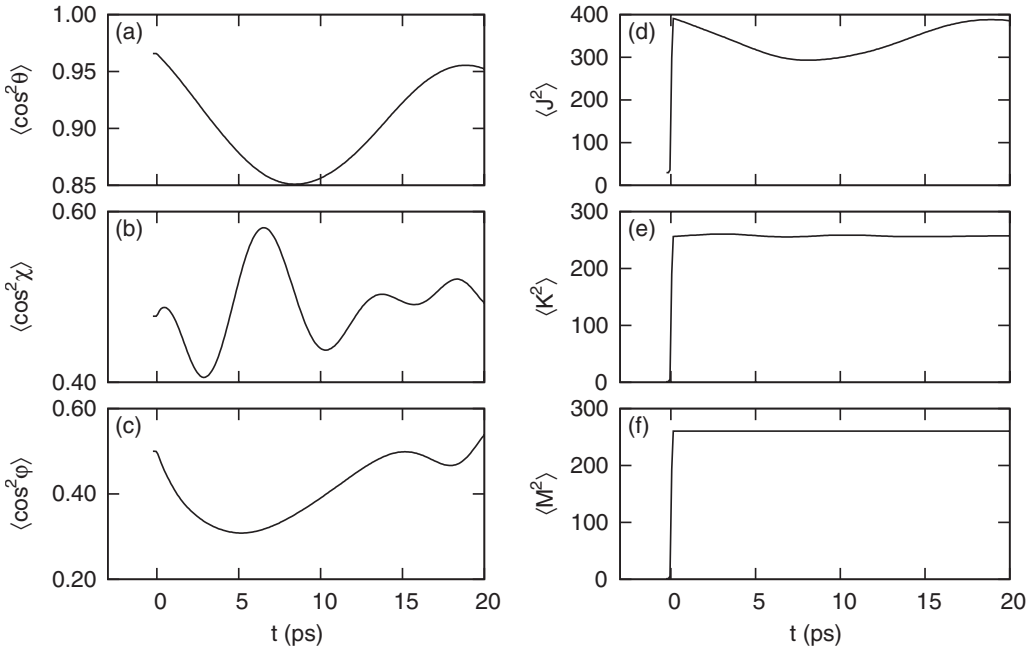

FIG. 5. Numerical simulation of 3D rotational alignment of DFIB. The intensities of the long and short pulses are $I_{long}=1.4\times10^{11}$ W/cm^2 and $I_{short}=2\times10^{13}$ W/cm^2, respectively, the short-pulse duration is 150 fs, and the rotational temperature is 0.2 K.

lar plane is aligned along the short-pulse polarization. To test if the initial alignment of the C-I axis is distorted by the short pulse, we turn to the I^+ images. At $t=3$ ps the I^+ distribution, recorded in the end view (Fig. 2 B4), has become slightly elliptical along the short-pulse polarization indicating that the C-I axis has suffered a minor distortion. This occurs due to the unavoidable imperfect 1D alignment induced by the long pulse that results in incomplete elimination of the interaction between the short pulse and the most polarizable axis (the C-I axis). The distortion of the C-I axis is, however, minor as seen by the fact that the I^+ image at $t=3$ ps is much better confined than the image recorded without the long pulse. We conclude that the C-I axis remains strongly aligned at $t=3$ ps and, consequently, that strong 3D alignment occurs at this time.

At times larger than 3 ps the F^+ ion confinement gradually disappears and at $t=8$ ps (Fig. 2 D5) the pre-kick circular symmetry is restored, followed by mild confinement along the x axis at $t=10$ ps (Fig. 2 D6). This evolution from alignment to antialignment of the plane is also visible in the F^+ side view. Here planar alignment at 3 ps manifests itself as two localized areas centered along the z axis (Fig. 2 C4). The antialignment confines the molecular plane to the detector plane (x,z) and produces a four-center F^+ image (Fig. 2 C6).

In Fig. 5 we complement our experiments with numerical simulations of the early alignment dynamics. Figures 5(a)–5(c) illustrate the expectation values of $\langle\cos^2\theta\rangle$, $\langle\cos^2\chi\rangle$, and $\langle\cos^2\phi\rangle$, respectively, where χ and ϕ are the azimuthal angles of rotation about the body- and space-fixed z axes, respectively (see Fig. 1). Figures 5(d)–5(f) provide the expectation values of $\hat{J}^2$, $\hat{K}^2$, and $\hat{M}^2$ in the rotational wave packet, respectively. Thus, Figs. 5(a)–5(c) quantify the alignment dynamics whereas Figs. 5(d)–5(f) quantify the underlying rotational excitation and connect coordinate space with the conjugate quantum number space. The zero of time is chosen, as in Fig. 2, at the center of the long and short pulses.

The long pulse produces sharp alignment of the molecular Z axis (C-I axis) to the space-fixed z axis, as evidenced by the expectation value $\langle\cos^2\theta\rangle=0.97$ [Fig. 5(a)]. The strong alignment is brought about by substantial coherent rotational excitation, $\langle J^2\rangle\sim400$ [Fig. 5(d)]. The subsequent short pulse produces rapid antialignment in χ, $\langle\cos^2\chi\rangle=0.4$ ($t=3$ ps), and later in ϕ, $\langle\cos^2\phi\rangle=0.3$ ($t=5$ ps). The antialignment in χ is followed by an alignment at 6 ps with $\langle\cos^2\chi\rangle=0.59$. Similary to the experimental results, the short pulse slightly perturbs the alignment in θ, leading to a decrease in the value of $\langle\cos^2\theta\rangle$ to 0.85 at 8 ps. The $\hat{J}^2$ and $\hat{K}^2$ expectation values undergo small-amplitude fluctuations after the short pulse turn-off because in the H_{adiab} representation J and K are not conserved quantum numbers. Figure 5 complements the numerical study of Ref. [25], which is not reproduced in the present paper, and the experimental study of Fig. 2. In Fig. 4 of Ref. [25] we chose the ratio of the long- and short-pulse intensities as in the experiment, and hence, with the short-pulse duration being equal in the numerical and experimental studies, the ratio of the field-matter interaction was the same, leading to good agreement. In Fig. 5 the short-pulse intensity is increased with respect to the study of [25], and hence, while the qualitative features of the alignment are not altered, the details are. It is important to note that our definition of the axis systems differs from the one we used in [25] for the numerical reasons discussed in Sec. II. With the present choice of the space-fixed z and y axes as the field polarization directions of the long and short pulses, an alignment of the second most polarizable molecular axis (X) with the space-fixed y axis (while the molecular Z axis is sharply aligned with the space-fixed z axis) corresponds to an anti-

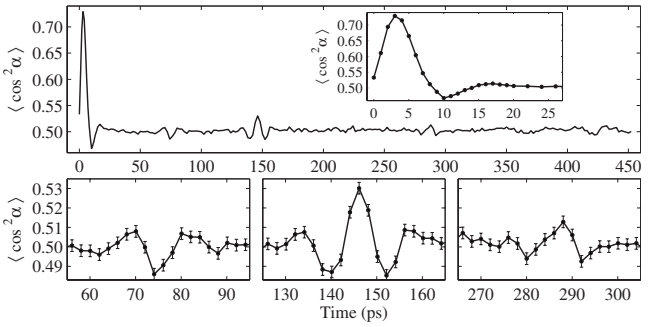

FIG. 6. Alignment dynamics of the molecular plane, represented by $\langle \cos^2 \alpha \rangle$, as a function of time after the short pulse. The laser intensities are the same as those given in Fig. 2. The inset and the three lower subfigures are magnified portions of the long scan.

alignment in χ (we follow the Euler angle definitions of Ref. [33]). Conversely, in interpreting the experimental results, an alignment of the molecular X axis to the short-pulse polarization direction constitutes an alignment in the angle α (α being the angle between the projection of the F^+ ion velocity vector on the detector plane and the short-pulse polarization vector).

C. Long-time dynamics and rotational revivals

The early-time dynamics discussed above show that the long pulse is capable of holding the C-I axis confined while the short pulse forces the plane to rotate about this axis. The immediate question arising is whether the hold-and-spin scheme leads to reconstruction of the initial alignment of the molecular plane at much longer times, similar to the rotational revivals observed in 1D alignment [27]. To answer this question we repeated the measurements for times out to ~450 ps. The results derived from F^+ end view images are summarized in Fig. 6, where we measure the degree of planar alignment $\langle \cos^2 \alpha \rangle$. It has a value of 0.5 for random orientation and reaches 1 and 0 in the limits of perfect alignment and antialignment, respectively. At the strong planar alignment maximum, $t=3$ ps, $\langle \cos^2 \alpha \rangle = 0.73$, whereas at the point of antialignment, $t=10$ ps, it decreases to 0.47. Subsequently, $\langle \cos^2 \alpha \rangle$ is essentially flat with a value of 0.50 except for four transients centered at 74, 146, 217, and 288 ps. At the strongest transient ($t=146$ ps), where $\langle \cos^2 \alpha \rangle$ reaches a maximum value of 0.53, the initial planar alignment is restored although with reduced strength. End view images of the I^+ ions in the time interval around this transient are essentially indistinguishable from those obtained without the short pulse, i.e., the long pulse keeps the C-I axis strongly confined. We conclude that 3D alignment exhibits revivals, corresponding, however, to much weaker planar confinement than the maximum at 3 ps.

A further analysis of the positions of the transients shows that the transients at 3, 146, and 288 ps, which have similar shapes, are repeated periodically with a separation of ~143 ps. This result is readily interpreted by noting the rotational constants of DFIB, as estimated in an independent rotational coherence spectroscopy experiment [34]. In particular, $A_e = 1750$ MHz is consistent with a period for rotation of the molecular plane about the molecular symmetry axis at $1/(4A_e) = 143$ ps. The positions of the weak transients observed between the major transients classify them as half revivals. These arguments are substantiated by quantum mechanical calculations below.

The long-time dynamics of the F^+ ions in the end view were also recorded without the long pulse. As expected, the pronounced 1D-like revivals observed in Fig. 6 disappear. This corroborates the picture of the long pulse keeping the C-I axis fixed while the short pulse induces a coherent rotational motion of the molecular plane. Under our experimental conditions the spinning of the molecule around the C-I axis is maintained for at least two full rotational periods. A weak structure is observed around $t=432$ ps, which would correspond to the third 1D-like revival.

The revival structure of the rotational wave packet of Fig. 5 in 3D angular space is illustrated by numerical calculations in Fig. 7. As in Fig. 5 above, the rotational dynamics is quantified by means of transferable parameters that are independent of the probe, but we show below that these parameters correspond closely to the experimentally measurable expectation values.

In particular, under our conditions of nearly perfect alignment of the molecule-fixed Z axis (C-I axis) to the space-fixed z axis (the long-pulse polarization vector), the experimentally measurable angle α conveys essentially the same information as the azimuthal angle χ, which rigorously describes rotation about the body-fixed Z axis. The short pulse causes $\langle \cos^2 \theta \rangle$ to oscillate about, and eventually ring down to, the value of 0.9. These oscillations are also reproduced in the $\hat{J}^2$ expectation value. $\langle \cos^2 \chi \rangle$ exhibits a periodic revival structure, corresponding to nearly regular, uniform rotation of the ensemble of molecules about the molecular axis. With the parameters used in this numerical simulation, i.e., the intensities of the two pulses and the initial thermal distribution of the H_{adiab} states corresponding to the rotational temperature of 0.2 K, the alignment in χ obtained upon turn-off is reproduced at the first revival. Experimentally, the amplitude of the first revival is strongly reduced compared to the alignment maximum at early times. The difference is due to the much sharper C-I axis alignment in the numerical results.

Figure 8 depicts the distribution of the rotational states before and after the short pulse. The bottom panel juxtaposes the initial thermal distribution of rotational states produced by the long pulse and the distribution of states at the end of the simulation ($t=450$ ps). Since the populations of the J levels oscillate after the short pulse turn-off, the latter distribution serves merely as an illustration of the overall breadth of the rotational wave packet produced by the short pulse. The top panel shows the same wave packet in terms of the coefficients of the H_{adiab} eigenstates plotted against the corresponding eigenvalues. Figure 8 complements Figs. 7(d)–7(f) in demonstrating a considerably larger extent of rotational excitation effected by the short pulse compared to the long pulse.

D. Role of the degree of 1D alignment

Figure 9 illustrates the numerical short-time 3D alignment for two intensities of the long pulse, keeping all other param-

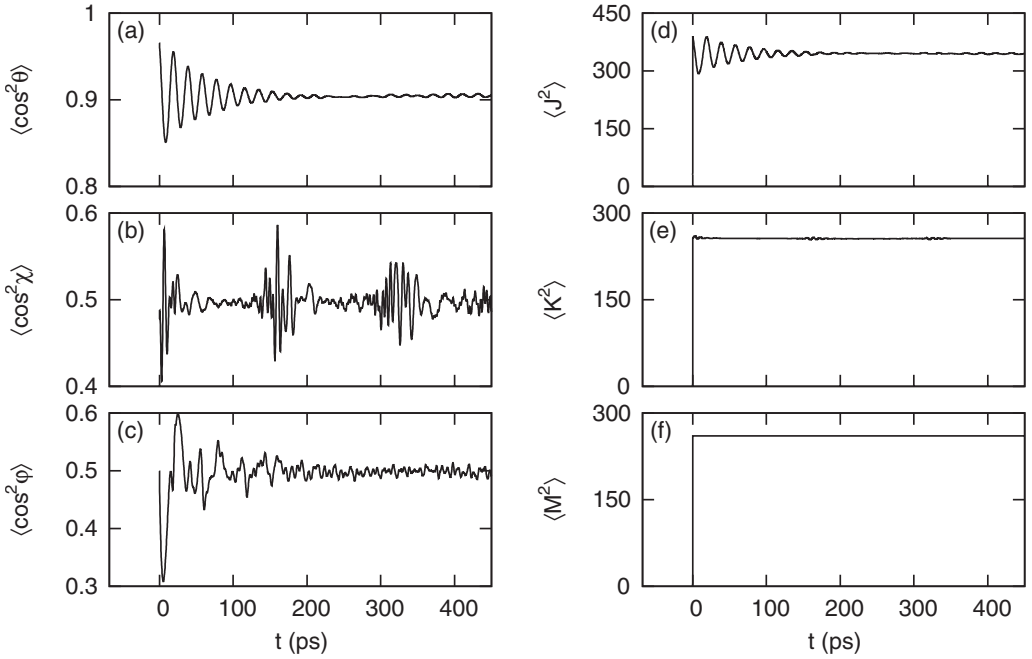

FIG. 7. Numerical simulation of the rotational revival dynamics of DFIB. The system and field parameters are as in Fig. 5.

eters as in the calculation of Fig. 5. Figures 9(a)–9(c) show the expectation values of $\langle\cos^2\theta\rangle$, $\langle\cos^2\chi\rangle$, and $\langle\cos^2\phi\rangle$, while Figs. 9(d)–9(f) show the expectation values of the corresponding conjugate quantum numbers. As illustrated in Figs. 9(b) and 9(c), the alignment of the two azimuthal angles is rather similar in the two cases. The early (0–12 ps) dynamics is barely distinguishable, whereas at longer times a small difference is observed. By contrast, the θ alignment shows a marked intensity effect. The initial 1D alignment induced by the long pulse is only slightly lower at the lower intensity $\langle\cos^2\theta\rangle=0.95$ compared to 0.97, but a major effect is seen in the longer-time response. In particular, the short pulse perturbs the alignment of the molecular Z axis to a greater extent as the long pulse intensity is lowered and the

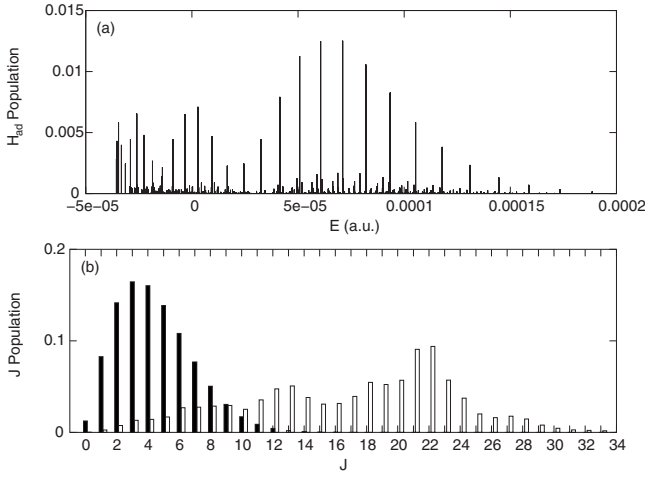

FIG. 8. (a) Distribution of the adiabatic Hamiltonian eigenstates produced by the short pulse. (b) Distribution of the rotational states before the short pulse (filled bars) and at the end of the simulation (empty bars).

1D alignment it induces degrades. As seen in Fig. 9, the alignment minimum decreases from $\langle\cos^2\theta\rangle=0.85$ to 0.71 and shifts from 8 to 12 ps.

The same conclusions are obtained experimentally. Figure 10 illustrates the results of an experiment similar to that discussed in the previous section, where all parameters are identical to those of Fig. 2, except for the long-pulse intensity, taken here to be 1.4×10^{11} W/cm^2. The end views of the F^+ ions are qualitatively similar to those recorded with the higher long-pulse intensity. In particular, the alignment dynamics of the plane, represented by $\langle\cos^2\alpha\rangle$, is almost identical to that obtained with the high intensity (see Fig. 2). Turning to the confinement of the C-I axis we note that prior to the short pulse the C-I axis is less confined than when the stronger long pulse is used. This is seen by the increased size of the I^+ distribution in the end view (compare Figs. 10 B1 and 2 B2) and by the decrease of $\langle\cos^2\theta_{2D}\rangle=$from 0.93 to 0.86 in the I^+ side view (compare Figs. 10 C1 and 2 A2).

Following the short pulse, a significant distortion of the confinement of the C-I axis is observed (Figs. 10 B2–10 B5). Since the short-pulse parameters are unchanged, the increased distortion can only result from lower initial confinement of the C-I axis. When comparing the most distorted ion images (Figs. 10 B3–10 B5) to the image recorded on nonaligned molecules (Fig. 2 B1), the confinement of the C-I axis along the vertical axis seems to have been almost lost. The I^+ side view confirms that there is a distortion but the very small amount of I^+ ions near the center also shows that the distortion is not severe.

Quantitative measures of the degree of alignment obtained with both the strong and the weak long pulse are presented in Fig. 11. The bottom graph shows the confinement of the molecular plane. Only small changes are observed when the intensity of the long pulse is changed. Clearly, the position of the initial alignment peak and that of the revival are unchanged while the degree of alignment ex-

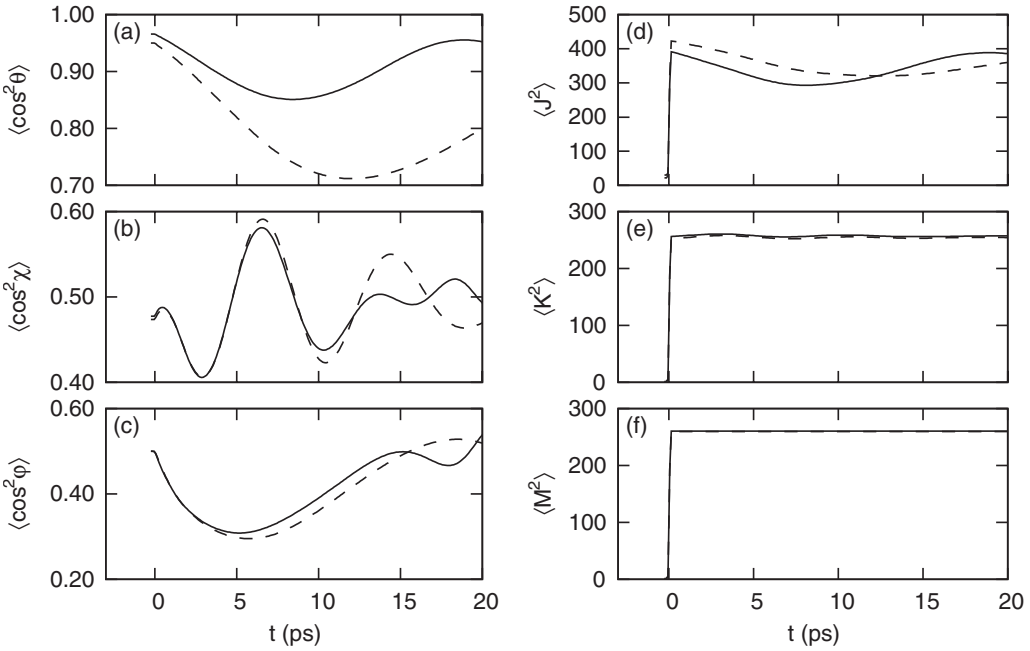

FIG. 9. Numerical simulations of the alignment of DFIB for two intensities of the long pulse: 1.4×10^{11} (solid) and 7×10^{10} W/cm^2 (dashed). The short-pulse intensity is kept at 2×10^{13} W/cm^2. The main effect of decreasing the long pulse intensity (thus the quality of the 1D adiabatic alignment) is in enhancing the perturbation of the long-pulse-induced alignment by the short pulse.

hibits small modification. By contrast, for the C-I axis alignment (top graph in Fig. 11) large differences are observed.

The top graph in Fig. 11 depicts the average pixel distances $\langle x\rangle$ and $\langle y\rangle$ from the ion hits to the center x axis and y axis, respectively (Fig. 10 B6). In the absence of the short pulse, the average distance to the center at the high intensity is around 44 pixels for both directions whereas for the low intensity it is 61 and 58 pixels along the vertical (y) and horizontal (x) axes, respectively (values extracted from Figs. 2 B2 and 10 B1). The asymmetry in the low-intensity case is due to a slightly elliptical long-pulse polarization. Following the short pulse the average distances remain relatively well controlled at high intensity, with a maximum increase of 10 pixels along y at $t=4$ ps. For the low-intensity case the impact is significantly higher, peaking along y at $t=7$ ps with an increase of 22 pixels. This shows that the interaction between the short pulse and the C-I axis is not negligible. In fact, at $t=7$ ps the average distance along y is 1 pixel higher than for the unaligned case (Coulomb explosion probe only: $\langle y\rangle=82$ and $\langle x\rangle=82$). Direct comparison, however, cannot be made since the Coulomb explosion probe possesses angular selectivity and the angular distributions are very different for the two images. For both the high and the low intensity, a decrease in the average distance is observed along the x axis.

As stated earlier, no structure is observed in the I^+ end view at long delays, which is clearly seen in the depicted interval around the revival at $t=146$ ps. Here the average distances are constantly 3–4 pixels higher that the value recorded in the absence of the short pulse.

Figures 9–11 lead to the same conclusions, namely, tight confinement of the most polarizable molecular axis prior to

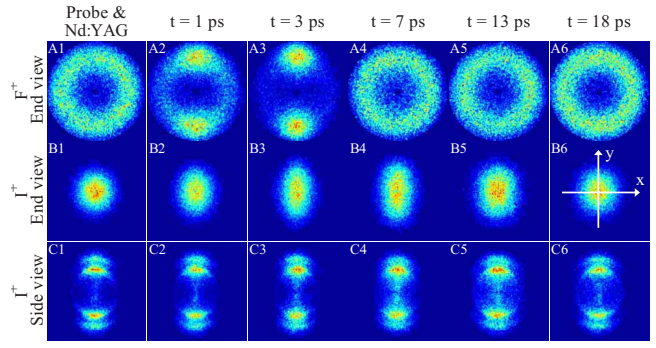

FIG. 10. (Color online) End view images (as recorded by the CCD camera) of F^+ fragments and both end and side view images of I^+ fragments. The long pulse intensity is 1.4×10^{11} W/cm^2. The x and y axes shown in B6 bisect the image center and are used to quantify the degree of alignment (see text).

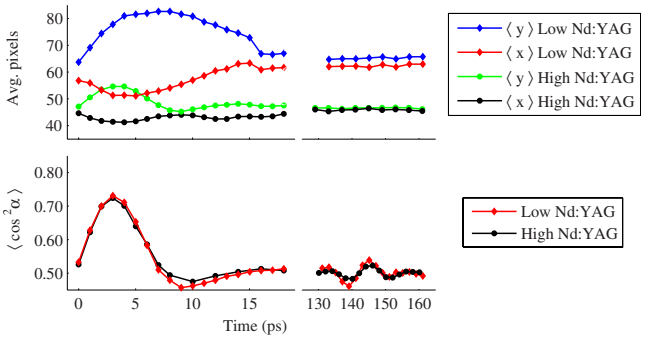

FIG. 11. (Color online) Top: Average distance to center along vertical axis (y) and horizontal axis (x) for each ion hit in the I^+ end view images. Bottom: $\langle\cos^2\alpha\rangle$ calculated from F^+ end view images. The intensity of the short pulse is fixed at 2×10^{13} W/cm^2, the long-pulse intensity is 7×10^{11} W/cm^2 in the "high intensity" series (black and green curves, circles) and 1.4×10^{11} W/cm^2 in the "low intensity" series (red and blue curves, diamonds).

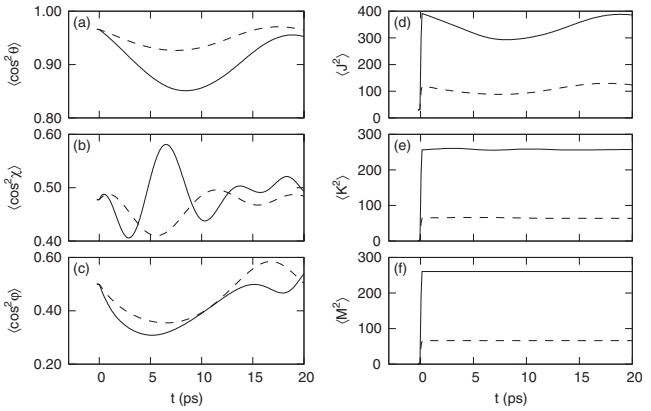

FIG. 12. Numerical simulations of the rotational alignment of DFIB for two short-pulse intensities: 2×10^{13} (solid) and 1×10^{13} W/cm^2 (dashed). The long pulse intensity is kept at 1.4×10^{11} W/cm^2.

the short pulse is essential for obtaining a high degree of 3D alignment. 3D alignment followed by a series of revivals of the rotation about the molecular axis will always be obtained through the hold-and-spin method, but the alignment of the most polarizable axis is deteriorated to a greater extent by the short pulse, the weaker the initial 1D alignment.

E. Role of the short-pulse fluence

In the sudden limit of 1D alignment, the degree of rotational excitation, and hence of molecular alignment, is fully determined by the fluence of the linearly polarized alignment pulse, that is, the same enhancement of the alignment can be obtained by either increasing the intensity or increasing the pulse duration by a given factor. This simple scaling of 1D nonadiabatic alignment is well understood [35]: In the short-pulse limit, the number of rotational levels coherently excited is essentially the number of Rabi cycles contained in the laser pulse, while the duration of the Rabi cycle scales inversely with the pulse intensity.

To the extent that the hold-and-spin approach introduced in the previous sections converts the rotation about the molecular axis into simple 1D-like motion, we expect the revival features of $\langle\cos^2\chi\rangle$ to scale with the laser fluence. Figure 12 illustrates the same set of expectation values as Fig. 5 for two values of the short-pulse intensity, the one used in Fig. 5 and a lower one. The lower-intensity short pulse produces considerably less rotational excitation [Figs. 12(d)–12(f)] than the higher-intensity one, and perturbs the θ alignment [Fig. 12(a)] to much lesser extent. The χ antialignment peak shifts from at 3 to ~6 ps while the alignment peak at 6 ps disappears. Similarly, the extent of the early ϕ antialignment is reduced from $\langle\cos^2\phi\rangle=0.3$ to 0.35. These results agree remarkably well with our expectation for 1D-type field-free alignment, corresponding to alignment of the azimuthal angle in a system where the molecular Z axis is essentially fixed.

We proceed by examining the effect of the short-pulse intensity on the experimental images. Figure 13 illustrates the results of an experiment similar to that described in Fig. 2, where, however, the short-pulse intensity is halved. For direct comparison of the experimental results for the two fluence values, we present in Fig. 13 also the high-fluence case of Fig. 2. Without the short pulse, the average pixel distances to the center are $\langle y\rangle=50$ pixels, $\langle x\rangle=47$ pixels, and $\langle\cos^2\alpha\rangle=0.512$. The asymmetric average pixel distances and the elevated $\langle\cos^2\alpha\rangle$ value result from slight misalignment of the polarization controlling wave plates. The long pulse was therefore not perfectly linear but rather slightly elliptically polarized. From Fig. 13 we see that the impact on the alignment of the C-I axis is only slightly reduced when the short-pulse intensity is lowered by a factor of 2. For both intensities the asymmetry peaks at $t=4$ ps with an average pixel value along y of 57 and 59 pixels for the low and high short-pulse fluences, respectively. At the lower fluence, a slightly slower evolution of the confinement of the molecular plane is observed in the F^+ end view images but the trace is similar to that observed at the high fluence. We attribute this result to a saturation of the alignment [36].

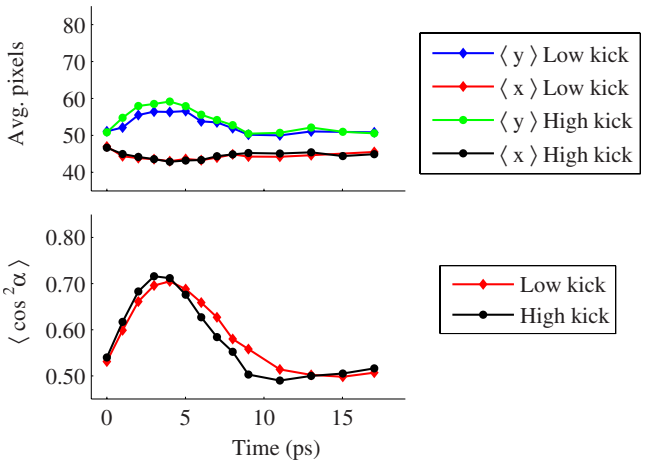

FIG. 13. (Color online) Top: Average distance to center along vertical axis (y) and horizontal axis (x) for each ion hit in the I^+ end view images. Bottom: $\langle\cos^2\alpha\rangle$ calculated from F^+ end view images. The intensity of the long pulse was fixed at 7×10^{11} W/cm^2 while the intensity of the short pulse was 2×10^{13} W/cm^2 in the "high kick" series (black and green curves, circles) and 1×10^{13} W/cm^2 in the "low kick" series (red and blue curves, diamonds)

F. Extension to field-free 3D alignment

Figure 14 illustrates numerically that truncation of the long pulse after the short pulse furnishes field-free 3D alignment, where the motion in all three Euler angles is spatially localized under field free conditions. The solid (red) curve of Fig. 14 provides the field-free results whereas the dashed (blue) curve compares these results with the alignment dynamics obtained in a similar experiment, where, however, the long pulse is not truncated and the revival dynamics takes place in the presence of the strong field.

The picture suggested by Figs. 5 and 14 is simple and general. The adiabatic turn-on populates a broad superposition of high-J states [Fig. 5(d)], conserving the space-fixed projection of J. The short pulse tilts the angular momentum vector with respect to the body-fixed and the space-fixed

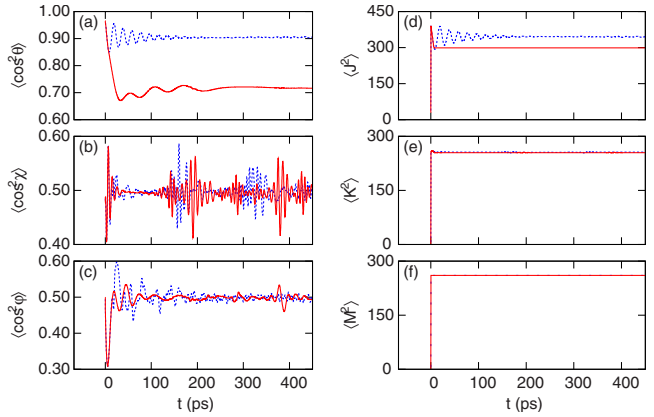

FIG. 14. (Color online) Alignment subsequent to truncation of the long pulse (solid red curve). The long- and short-pulse intensities and the short-pulse duration are as in Fig. 5. The long pulse is turned off at $t=6.7$ ps within 100 fs. The results of Fig. 5 are reproduced here by the dashed (blue) curve for comparison.

frames through coherent excitation of M and K levels [Figs. 5(e) and 5(f)]. This leads to an initial minimum in the alignment of the symmetry axis, while the plane spanned by the two most polarizable molecular axes aligns with the plane spanned by the laser polarizations. After the short pulse, if the long pulse is not switched off, the symmetry axis alignment will again peak, while the plane alignment is gradually deteriorated. By truncating the long pulse rapidly (with respect to rotations), the plane alignment remains available, providing field-free 3D alignment. Our ability to time the truncation of the long pulse provides a handle on the ensuing field-free 3D alignment, as it allows tuning with precision the alignment in the three senses. Figure 14 is computed for DFIB but its conclusions are general. The next section and the supplementary material provide a complementary discussion of the truncated hold-and-spin approach applied to 3,4-dibromothiophene.

We remark that 1D field-free alignment by a rapidly switching off pulse has been illustrated numerically [37] and also demonstrated experimentally [20,38]. In the laboratory it can be realized on a 150 fs time scale, but it is theoretically understood that the turn-off time need only be short with respect to the rotational periods [39].

G. Molecular systems

We proceed to generalize our results by considering the application of the hold-and-spin approach to a rather different molecular system. As such we use 3,4-dibromothiophene, previously studied in the context of 3D adiabatic alignment by a long, elliptically polarized pulse [22]. We stress that the DBT experimental results were recorded prior to the experiments on DFIB, under less ideal experimental conditions, and are thus inferior to the DFIB results in quality. They nevertheless allow us to generalize some of our conclusions based on the DFIB study.

The DBT experiments were conducted in an older vacuum system using a Jordan Company valve rather than the high-pressure Even Lavie employed for the DFIB studies. Consequently, the rotational temperature of the DBT molecules is higher than the temperature in the DFIB measurements and, thus, the adiabatic alignment, induced by the long pulse, is weaker. The experimental observables are the S^+, recoiling primarily along the C_2 symmetry axis and the Br^+ ions, recoiling in the molecular plane.

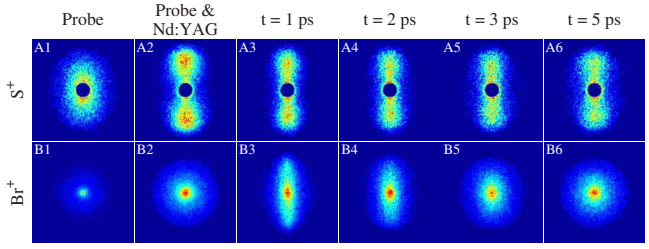

FIG. 15. (Color online) Ion images (as recorded by the CCD camera) from DBT of S^+ and Br^+. The durations and intensities were 10 ns and 1.4×10^{12} W/cm^2, 0.7 ps and 10×1.0^{13} W/cm^2, and 25 fs and 2.6×10^{14} W/cm^2 for the long, short, and probe pulses, respectively. The central part of the S^+ images has been removed to avoid displaying thermal O_2^+ ions, originating from ionization of chamber background.

A series of S^+ and Br^+ images, recorded at different times, are displayed in Fig. 15. The laser pulse parameters are given in the caption. For the S^+ ion images the long pulse and the probe pulse were polarized in the plane of the detector (vertically in the images) and the short pulse was polarized perpendicular to the plane of the detector. In the Br^+ ion images all polarizations were rotated by 90°, orienting the polarization of the long and the probe pulses perpendicular to the plane of the detector and the short pulse in the plane of the detector (vertically in the images). In analogy with the notation used for DFIB the S^+ ion images correspond to side views of the molecules and the Br^+ ion images to end views (provided the molecular C_2 symmetry axis is well aligned by the long pulse).

Figure 15 A1 shows the S^+ ion image when only the probe pulse is used. The minor angular localization along the probe polarization axis reflects the enhanced ionization rate for those DBT molecules that happen to have their C_2 symmetry axis oriented near the probe polarization at the time of ionization. When the long pulse is included (Fig. 15 A2), the angular localization sharpens, due to adiabatic alignment of the C_2 symmetry axis along the long pulse polarization. Turning to the Br^+ ions it is seen that the images with (Fig. 15 B2) and without (Fig. 15 B1) the long pulse are both circularly symmetric, similar to the DFIB experiment. When the short pulse is included, the Br^+ images change dramatically. At very early times (Fig. 15 B3) the ion distribution emerges as a narrow line along the direction of the short-pulse polarization. At longer times this confinement quickly disappears and a circularly symmetric distribution is restored already around $t=5$ ps. The observation at $t=1$ ps is only compatible with the Br^+ ions being ejected in the plane defined by the long- and the short-pulse polarizations, i.e., alignment of the molecular plane to the space-fixed plane, spanned by the polarizations of the two alignment pulses. The S^+ image at $t=1$ ps shows that the C_2 symmetry axis is still aligned along the long-pulse polarization (Fig. 15 A3).

Thus, we conclude that pronounced 3D alignment, corresponding to simultaneous confinement of the molecular plane and the C_2 symmetry axis to space-fixed axes, is achieved at $t=1$ ps.

From the top row of Fig. 15 it is clear that the short pulse disturbs the confinement of the C_2 symmetry axis. The changes are, however, hard to quantify experimentally, since no distinct radial recoil channels are observed for the S^+ ions. Also, at the time the DBT experiment was carried out, we had not yet realized the additional information content available in S^+ end views, so unfortunately images in this geometry were not recorded. Less disturbance of the S^+ images is observed when a four times weaker short pulse is employed (not displayed here). At this intensity (2.5×10^{12} W/cm^2), the strongest confinement of Br^+ image does not peak until $t=4$ ps as expected for the significantly weaker kick.

An extensive numerical study of the DBT 3D alignment induced by the combination of a long and a short pulse leads to similar conclusions as the DFIB study discussed above and the experimental results. Numerical illustrations are available in the supplementary material and only a brief summary is provided here.

Localization of all three Euler angles, and thus 3D alignment, is achieved for any choice of the short pulse intensity. The timing and extent of angular localizations in each of the three Euler angles depend on the relative strength of the interaction of the long and the short pulses with the molecule. The former is determined by the intensity of the long pulse, which (for a given rotational temperature), determines the degree of rotational excitation in the adiabatic limit. The latter is determined by the fluence of the short pulse, which determines the degree of rotational excitation in the nonadiabatic case [35]. Thus, as the ratio of the short-pulse fluence to the long-pulse intensity increases, the plane alignment improves at the expense of the axis alignment.

The questions of when and why the alignment quality of the primary axis will suffer substantial distortion in response to the second pulse are addressed, as above, by examining the dependence of $\langle \cos^2 \theta \rangle$ and $\langle \cos^2 \phi \rangle$ on the long-pulse intensity while keeping constant the ratio of the long- and short-pulse intensities and the short-pulse duration. We find (see the supplementary material [40]) that the quality of alignment measured in the azimuthal Euler angle coordinate ϕ is comparably good, although the use of a stronger short pulse causes the alignment to shift to earlier times. The loss of alignment in the major polarizability axis, however, depends crucially on the intensity, with lower-intensity long pulses demonstrating an inability to retain the alignment of the C_2 axis, and thus resulting in substantially lower-quality 3D alignment. The DBT results substantiate our conclusions based on the DFIB results, namely, the extent of 3D alignment relies on the presence of a strong adiabatic field, which serves to arrest the most polarizable molecular axis to the long-pulse polarization axis and minimizes the interaction of the molecular major polarizability axis with the short-pulse field.

Importantly, we include in the supplementary material [40] also a detailed account of the possibility of extending the hold-and-spin approach to obtain field-free 3D alignment of DBT, similar to that numerically demonstrated above for DFIB. We conclude from the numerical studies and theoretical considerations of the previous section and the supplementary material that field-free 3D alignment always obtains through the truncated hold-and-spin approach. The degree of alignment in each of the angles and the extent to which the alignment observed subject to the long pulse survives under field-free conditions, however, depend strongly on the molecular and field parameters.

IV. CONCLUSIONS

In the previous sections we extended an approach to controlled rotations of asymmetric top molecules, introduced in a recent Letter [25], in several ways. First, we expanded our previous discussion of the principles of the hold-and-spin approach and substantiated the conclusions of Ref. [25]. Next we explored the role played by several of the parameters of the approach. In particular, we illustrated and explained the reliance of the method on our ability to produce tight 1D alignment using the long pulse. We remark that this requires a large ratio of the laser-induced potential to the rotational energy. Since the laser intensity is upper-limited by the onset of nonresonant ionization, attaining a sufficiently large ratio requires a low rotational temperature. Finally, we generalized the discussion of Ref. [25] by considering two asymmetric top molecules that differ widely in properties. In numerical work, we demonstrated also the extension of the method to field-free 3D alignment by truncation of the long pulse subsequent to the short-pulse turn-off.

As a route to transient 3D alignment, the hold-and-spin approach provides unprecedented 3D alignment after the short pulse. As an approach to controlling the rotations of polyatomic molecules it introduces a means of converting the complex wobbling motion of asymmetric tops into nearly regular 1D rotation with an intuitive classical analog.

One of our goals in future research will be the generalization of the hold-and-spin method to control the torsional motions of polyatomic molecules. Ultimately, we hope to be able to extend our methods to increasingly complex systems of chemical and materials science interest.

ACKNOWLEDGMENTS

This work was supported by the U.S. Department of Energy, the Carlsberg Foundation, the Lundbeck Foundation, and the Danish Natural Science Research Council. This research used resources of the National Energy Research Scientific Computing Center, which is supported by the Office of Science of the U.S. Department of Energy under Contract No. DE-AC02-05CH11231.

[1] R. A. Bartels, T. C. Weichnact, N. Wagner, N. Baertschy, C. H. Greene, M. M. Murnane, and H. C. Kapteyn, Phys. Rev. Lett. **88**, 013903 (2002).
[2] J. Spence, K. Schmidt, J. Wu, G. Hembree, U. Weierstall, B. Doak, and P. Fromme, Acta Crystallogr., Sect. A: Found. Crystallogr. **61**, 237 (2005).
[3] E. Peterson *et al.*, Appl. Phys. Lett. **92**, 094106 (2008).
[4] J. Itatani, J. Levesque, D. Zeidler, H. Niikura, H. Pépin, J. C. Kieffer, P. B. Corkum, and D. M. Villeneuve, Nature (London) **432**, 867 (2004).
[5] M. Meckel *et al.*, Science **320**, 1478 (2008).
[6] T. Kanai, S. Minemoto, and H. Sakai, Nature (London) **435**, 470 (2005).
[7] C. Vozzi *et al.*, Phys. Rev. Lett. **95**, 153902 (2005).
[8] C. B. Madsen, A. S. Mouritzen, T. K. Kjeldsen, and L. B. Madsen, Phys. Rev. A **76**, 035401 (2007).
[9] Y. Mairesse *et al.*, New J. Phys. **10**, 025028 (2008).
[10] S. Ramakrishna and T. Seideman, Phys. Rev. Lett. **99**, 103001 (2007).
[11] M. D. Poulsen, E. Péronne, H. Stapelfeldt, C. Z. Bisgaard, S. S. Viftrup, E. Hamilton, and T. Seideman, J. Chem. Phys. **121**, 783 (2004).
[12] K. F. Lee, D. M. Villeneuve, P. B. Corkum, A. Stolow, and J. G. Underwood, Phys. Rev. Lett. **97**, 173001 (2006).
[13] A. Rouzèe, S. Guèrin, V. Boudon, B. Lavorel, and O. Faucher, Phys. Rev. A **73**, 033418 (2006).
[14] S. Ramakrishna and T. Seideman, Phys. Rev. Lett. **95**, 113001 (2005).
[15] M. Reuter, M. Sukharev, and T. Seideman, Phys. Rev. Lett. Phys. Rev. Lett. **101**, 208303 (2008).
[16] J. C. H. Spence and R. B. Doak, Phys. Rev. Lett. **92**, 198102 (2004).
[17] B. Friedrich and D. Herschbach, J. Chem. Phys. **111**, 6157 (1999).
[18] R. Baumfalk, N. H. Nahler, and U. Buck, J. Chem. Phys. **114**, 4755 (2001).
[19] H. Sakai, S. Minemoto, H. Nanjo, H. Tanji, and T. Suzuki, Phys. Rev. Lett. **90**, 083001 (2003).
[20] A. Goban, S. Minemoto, and H. Sakai, Phys. Rev. Lett. **101**, 013001 (2008).
[21] S. Guérin, A. Rouzée, and E. Hertz, Phys. Rev. A **77**, 041404(R) (2008).
[22] L. Holmegaard, J. H. Nielsen, I,. Nevo, H. Stapelfeldt, F. Filsinger, J. Küpper, and G. Meijer, Phys. Rev. Lett. **102**, 023001 (2009).
[23] J. J. Larsen, K. Hald, N. Bjerre, H. Stapelfeldt, and T. Seideman, Phys. Rev. Lett. **85**, 2470 (2000).
[24] J. G. Underwood, B. J. Sussman, and A. Stolow, Phys. Rev. Lett. **94**, 143002 (2005).
[25] S. S. Viftrup, V. Kumarappan, S. Trippel, H. Stapelfeldt, E. Hamilton, and T. Seideman, Phys. Rev. Lett. **99**, 143602 (2007).
[26] A. Rouzee, S. Guerin, O. Faucher, and B. Lavorel, Phys. Rev. A **77**, 043412 (2008).
[27] H. Stapelfeldt and T. Seideman, Rev. Mod. Phys. **75**, 543 (2003).
[28] T. Seideman and E. Hamilton, Adv. At., Mol., Opt. Phys. **52**, 289 (2006).
[29] M. D. Poulsen, T. Ejdrup, H. Stapelfeldt, E. Hamilton, and T. Seideman, Phys. Rev. A **73**, 033405 (2006).
[30] V. Kumarappan, C. Z. Bisgaard, S. S. Viftrup, L. Holmegaard, and H. Stapelfeldt, J. Chem. Phys. **125**, 194309 (2006).
[31] E. Hamilton, T. Seideman, T. Ejdrup, M. D. Poulsen, C. Z. Bisgaard, S. S. Viftrup, and H. Stapelfeldt, Phys. Rev. A **72**, 043402 (2005).
[32] L. Holmegaard, S. S. Viftrup, V. Kumarappan, C. Z. Bisgaard, H. Stapelfeldt, E. Hamilton, and T. Seideman, Phys. Rev. A **75**, 051403(R) (2007).
[33] R. N. Zare, *Angular Momentum* (Wiley, New York, 1988).
[34] S. S. Viftrup, Ph. D. thesis, Department of Physics and Astronomy, University of Aarhus, 2007.
[35] T. Seideman, J. Chem. Phys. **103**, 7887 (1995).
[36] M. Leibscher, I. Sh. Averbukh, and H. Rabitz, Phys. Rev. A **69**, 013402 (2004).
[37] Z.-C. Yan and T. Seideman, J. Chem. Phys. **111**, 4113 (1999).
[38] J. G. Underwood, M. Spanner, M. Yu Ivanov, J. Mottershead, B. J. Sussman, and A. Stolow, Phys. Rev. Lett. **90**, 223001 (2003).
[39] T. Seideman, J. Chem. Phys. **115**, 5965 (2001).
[40] See EPAPS Document No. E-PLRAAN-79-125901 for the 3D alignment results in the case of 3,4-dibromothiophene. For more information on EPAPS, see http://www.aip.org/pubservs/epaps.html.